Analysis of Instability in Torque Control of Sensorless PMSM Drives in Flux Weakening Region

Jiwon Yoo, *Student Member*, *IEEE*, Joohyun Lee, *Student Member*, *IEEE*, and Seung-Ki Sul, *Fellow*, *IEEE*

***Abstract*— This paper analyzes the effect of angle estimation error on the sensorless torque control of the permanent-magnet synchronous motor (PMSM). The actual torque of PMSM may differ from the torque reference due to the angle error in sensorless control. Furthermore, this torque discrepancy can cause instability to the control system, especially in the flux weakening region. The instability is highly dependent on the gain setting of the controller and observer in the control loop. To mitigate the adverse effect of the angle error, a torque feedforward method considering the transient angle error is proposed. With the proposed torque feedforward method, the gain margin of the control loop can be enhanced without modifying the gain of the control system. The proposed method is verified through the simulation and experimental results.**

***Index Terms*—Observer, permanent-magnet synchronous motor, sensorless drive, stability, torque control.**

NOMENCLATURE

$(\,)^{\mathbf{s}}_{\mathbf{dqs}} = \begin{bmatrix} (\,)^{s}_{ds} \\ (\,)^{s}_{qs} \end{bmatrix}$	*dq*-vector variable at stationary reference frame.
$(\,)^{\hat{\mathbf{r}}}_{\mathbf{dqs}} = \begin{bmatrix} (\,)^{\hat{r}}_{ds} \\ (\,)^{\hat{r}}_{qs} \end{bmatrix}$	*dq*-vector variable at estimated rotor reference frame.
$(\,)^{\mathbf{r}}_{\mathbf{dqs}} = \begin{bmatrix} (\,)^{r}_{ds} \\ (\,)^{r}_{qs} \end{bmatrix}$	*dq*-vector variable at rotor reference frame.
$(\hat{\ })$	Estimated value.
$(\,)^{*}$	Reference value.
$(\tilde{\ })$	Error between actual and estimated values.
$(\tilde{\hat{\ }})$	Estimated error.
θ_{rm}	Mechanical rotor angle.
θ_{r}	Electrical rotor angle.
ω_{rm}	Mechanical rotor speed.
ω_{r}	Electrical rotor speed.
p	Number of pole pairs.

I. INTRODUCTION

THE APPLICATIONS of the permanent-magnet synchronous motors (PMSMs) have been widened to various industries such as servo drives, home appliances, and hybrid/electric vehicles. Most PMSM drives adopt the field-oriented control (FOC) or the direct torque control (DTC) as their control scheme, and they require the information of the rotor position. Of course, a position sensor can be installed on the rotor shaft, but it often increases the cost and may not be available due to mechanical reasons. To shed these limitations, the sensorless control technology that estimates rotor position without position sensor has been researched and commercialized in recent years [1]-[18].

Depending on what physical information is used for the angle estimation, the sensorless control technology can be categorized into two groups, which are the rotor saliency-based methods [1]-[8] and the model-based methods [8]-[15]. The rotor saliency-based methods exploit the saliency due to the rotor shape [2] or the partial magnetic saturation [4] by injecting an additional voltage/current signal. On the other hand, the model-based methods estimate the rotor position using the back-electromotive force (back-EMF) of PMSM, which can be calculated from the terminal voltage and the electrical model of PMSMs.

No matter what type of sensorless method is taken, the primitive output of most sensorless techniques is not the rotor angle itself but the rotor angle error, which is the difference between the estimated rotor angle and the actual rotor angle. In order to obtain actual rotor angle information from the angle error, position estimators such as a PI-based phase locked loop (PLL) [5], [8], [9], [13] or state observer [1], [6], [14]-[19] have been used. Some research works have reported the sensorless observers which directly estimate the rotor angle, instead of angle error [14], [18]. However, even in those research works, the position estimator was adopted to eliminate the noise in the angle estimation and to obtain the rotor speed information. Thus, the position estimator cascaded with the sensorless observer is the common structure in sensorless PMSM control.

Although various types of position estimators have been proposed, their basic principle is to estimate the rotor angle that makes the estimated angle error be null. Therefore, the angle error converges to zero in steady-state under the sensorless control with the accurate motor parameters [11]-[13]. However, there is an inevitable angle error in the transient state due to the limited bandwidth of the position estimator [14]- [19].

To enhance the dynamics of the position estimator, the torque reference was used as a feedforward term in the state observer type position estimator [16], [17]. Feedforwarding torque

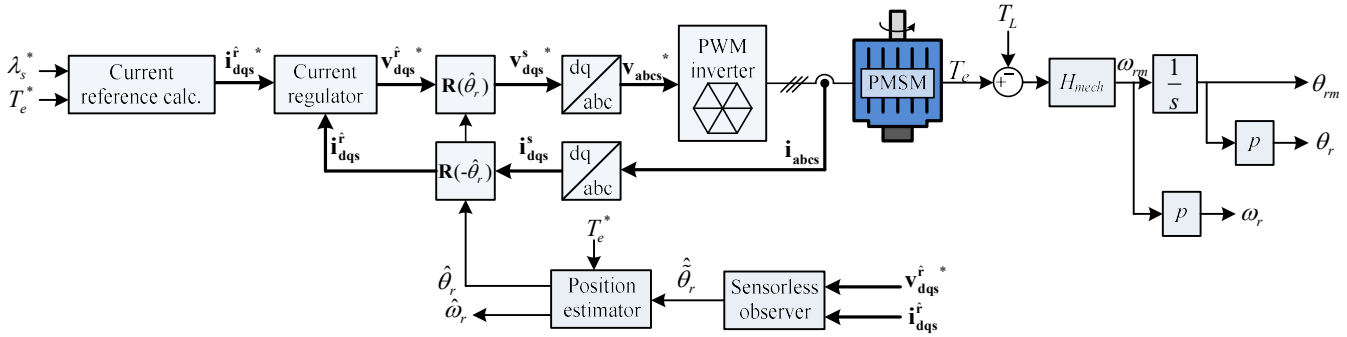

Fig. 1. Block diagram of sensorless torque control.

reference can virtually extend the bandwidth of the position estimator, and the transient angle error due to torque reference change can be conspicuously reduced.

However, the angle error causes an error between the actual torque and its reference. The angle error directly leads to the discrepancy between the rotor reference frame (RRF) and the estimated RRF (ERRF). Considering that the output torque corresponds to the current vector at RRF and the current control of the drive system works at ERRF, the angle error can deteriorate the torque accuracy. Furthermore, an unidentified load torque also disturbs the angle estimation. Therefore, feedforwarding torque reference is not enough to eliminate the angle error.

The inevitable error in angle estimation can affect the stability of the drive system. As the torque discrepancy due to angle error is input to the mechanical system, the speed oscillation would occur. Depending on the gain setting of the system and the mechanical characteristics, the speed oscillation caused by angle error may not be attenuated but make the control system unstable.

In this paper, it is analyzed how the angle error affects the stability of the drive system. First, the torque error due to the angle error is calculated depending on the operating points. Because of this torque error, an undesired feedback term is generated in the sensorless torque control. And, it is analyzed how this unwanted feedback term changes the pole locations of the control loop. Especially in the flux weakening (FW) operation, it is revealed that the poles of the control system may migrate to the unstable region.

This phenomenon can be more severe in low-inertia applications or when the gains of the position estimator are not large enough. However, since the position estimator gains are directly related to the bandwidth of the estimator, it is limited by the desired noise immunity of the target system. Therefore, increasing the gains of the position estimator is not always a feasible solution for every industry application. Alternatively, this paper proposes a torque feedforward method considering the error in angle estimation. The proposed compensation method ensures the stability of the system without increasing the gains of the observer, which keeps the same noise immunity in the high-frequency region as the conventional system does. The feasibility of the proposed method is verified with a series of simulation and experimental tests.

In addition to the previously presented paper [19], this paper

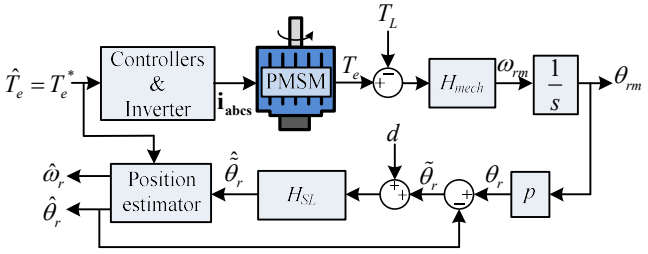

Fig. 2. Simplified block diagram of sensorless torque control system.

provides the following.

1) Detailed analysis of the stability condition.
2) Noise immunity analysis of the proposed method.
3) Simulation and experimental results under parameter errors and those in speed control mode.

II. Stability of Sensorless Torque Control

A. Small-Signal Model of Sensorless PMSM Drives

When a PMSM operates in the sensorless control mode, the torque control block diagram can be illustrated as Fig. 1. θ_{rm} and ω_{rm} represent the rotor angle and speed in mechanical angle. θ_r and ω_r stand for those in electrical angle, respectively. p is the number of pole pairs. $\mathbf{R}(\theta)$ denotes the rotation matrix which is

$$\mathbf{R}(\theta)=\begin{bmatrix}\cos\theta & -\sin\theta\\ \sin\theta & \cos\theta\end{bmatrix}. \tag{1}$$

The current reference $\mathbf{i}^{\hat{r}*}_{dqs}$ can be calculated corresponding to the torque reference T_e^* and the stator flux reference λ_s^*. Through the current controller and PWM inverter, the stator current $\mathbf{i}^{s}_{dqs}$ is regulated, and the actual torque T_e is produced. T_e can be treated as the input to the mechanical system H_{mech}, which has a disturbance of load torque T_L. In this paper, H_{mech} is assumed as a single-pole system with free inertia J_m and friction constant B_m, as follows.

$$H_{mech}=\frac{1}{J_m s+B_m}. \tag{2}$$

The typical sensorless observers, such as the extended back-EMF method [9] or the full-order observer [11], [12], take dq-axes voltages and currents as input variables and calculate the

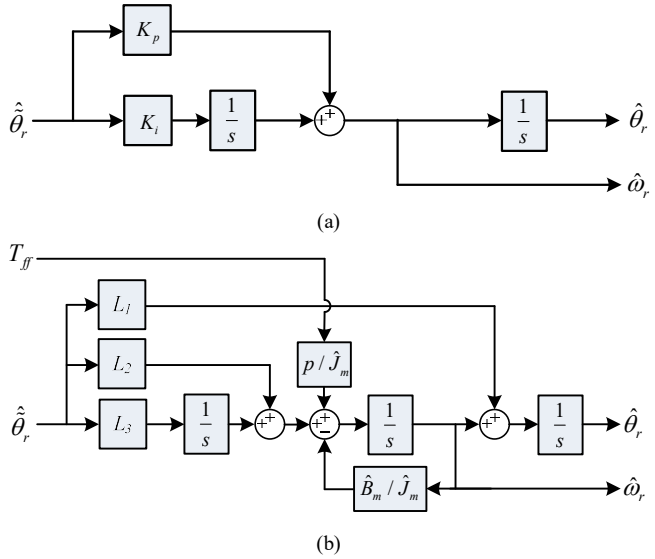

Fig. 3. Block diagrams of position estimator. (a) PI-PLL. (b) ESO.

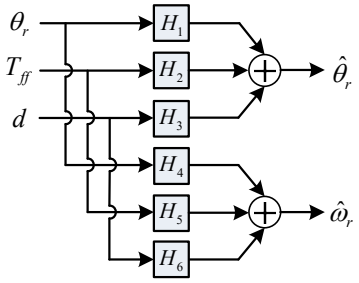

Fig. 4. Transfer function of ESO.

estimated angle error $\hat{\tilde{\theta}}_r$. The estimated rotor angle $\hat{\theta}_r$ and the speed $\hat{\omega}_r$ are obtained from the estimated angle error $\hat{\tilde{\theta}}_r$ through the position estimator. Focusing on the relation between $\hat{\tilde{\theta}}_r$ and the actual angle error, $\tilde{\theta}_r = \theta_r - \hat{\theta}_r$, the sensorless control system can be simplified as Fig. 2. $\hat{\tilde{\theta}}_r$ calculated from the sensorless observer using the voltage and current signals reflects $\tilde{\theta}_r$, but may have an error due to the nonideal operation of the sensorless observer. In Fig. 2, the phase delay and magnitude distortion of $\hat{\tilde{\theta}}_r$ compared to $\tilde{\theta}_r$ are represented by H_{SL}, equivalently. Similarly, the offset and noise in $\hat{\tilde{\theta}}_r$, caused by the sensorless observer, are indicated by d. If the sensorless observer is ideal without delay and magnitude error, H_{SL} becomes the unity.

The rotor angle and speed can be estimated by a position estimator. While there are various types of position estimators, PI-based PLL (PI-PLL) and the extended state observer (ESO) in Fig. 3 have been common solutions. K_p and K_i in Fig. 3 (a), and L_1, L_2, and L_3 in Fig. 3 (b) are the gains of each position estimator, and T_{ff} stands for the torque feedforward term in ESO. In Fig. 3 (b), $\hat{J}_m$ and $\hat{B}_m$ denote the estimated mechanical inertia and friction constant. Although the gain setting and the implementation are more comfortable in PI-PLL, ESO has a

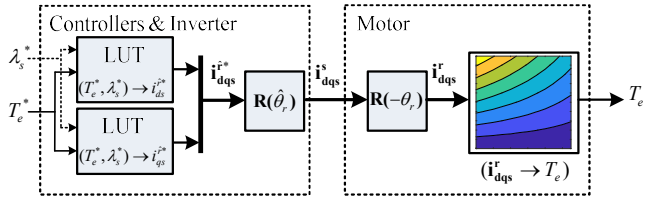

Fig. 5. Simplified block diagram of current control and motor.

better dynamic performance and noise rejection. In the following analysis, ESO is selected as the position estimator. The ESO can be considered as transfer functions from T_{ff}, θ_r, and d to $\hat{\theta}_r$ and $\hat{\omega}_r$, as shown in Fig. 4. In Fig. 4, $H_1 - H_6$ can be deduced as

$$\begin{bmatrix} H_1 & H_2 & H_3 \\ H_4 & H_5 & H_6 \end{bmatrix} = \begin{bmatrix} \frac{\hat{\theta}_r}{\theta_r} & \frac{\hat{\theta}_r}{T_{ff}} & \frac{\hat{\theta}_r}{d} \\ \frac{\hat{\omega}_r}{\theta_r} & \frac{\hat{\omega}_r}{T_{ff}} & \frac{\hat{\omega}_r}{d} \end{bmatrix} \tag{3}$$

where

$$H_1 = 1 - \frac{s(\hat{J}_m s^2 + \hat{B}_m s)}{\hat{J}_m H_{ch,ESO}} \tag{4}$$

$$H_2 = \frac{p \cdot s}{\hat{J}_m H_{ch,ESO}} \tag{5}$$

$$H_3 = H_1 \tag{6}$$

$$H_4 = \frac{(\hat{J}_m L_2 s^2 - L_3 s)}{\hat{J}_m H_{ch,ESO}} \tag{7}$$

$$H_5 = \frac{p \cdot s(s + L_1)}{\hat{J}_m H_{ch,ESO}} \tag{8}$$

$$H_6 = H_4 \tag{9}$$

$$H_{ch,ESO} = s^3 + \left(\hat{B}_m / \hat{J}_m + L_1\right)s^2 + \left(L_1 \hat{B}_m / \hat{J}_m + L_2\right)s + L_3 . \tag{10}$$

Generally, gains of ESO can be set as follows from $H_{ch,ESO}$. The parameters, ω_0, ω_n, and ζ_n, are set under the consideration of stable operation and reasonable dynamic performance of ESO.

$$H_{ch,ESO} = \left(s + \omega_o\right)\left(s^2 + 2\zeta_n \omega_n s + \omega_n^{\,2}\right) \tag{11}$$

where

$$L_1 = \omega_o + 2\zeta_n \omega_n - \hat{B}_m / \hat{J}_m \tag{12}$$

$$L_2 = \omega_n^{\,2} + 2\zeta_n \omega_n \omega_o - L_1 \hat{B}_m / \hat{J}_m \tag{13}$$

$$L_3 = \omega_o \omega_n^{\,2} . \tag{14}$$

In the derivation of (3)-(14), H_{SL} is assumed to be unity. It implies that the bandwidth of the position estimator is much lower than that of the sensorless observer, and the delay of the sensorless observer is negligible in the position estimator's point of view.

B. Torque Discrepancy Due to Angle Error

In the previous section, the mechanical system and the position estimator were represented by the transfer functions. Meanwhile, it can be noticed that there is no explicit feedback

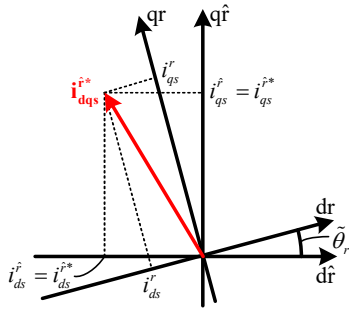

Fig. 6. Current vector diagram with an angle estimation error.

loop in Fig. 2. Therefore, if the current controller, inverter, and motor operate as an ideal torque actuator, which has the unity transfer function, the stability of the sensorless torque control of PMSM would be needless to be discussed. However, the non-ideal characteristics of the inverter and motor would perturb the stability of the control system. Especially in sensorless drives, the angle error makes the ideal operation more difficult.

As aforementioned, the current reference generator in Fig. 1 calculates $\mathbf{i}_{\mathbf{dqs}}^{\hat{\mathbf{r}}*}$ corresponding to T_e^* and λ_s^*. In this paper, it is assumed that the current reference is calculated through a precalculated look-up-table (LUT) [20], [21]. Under the assumption of a well-regulating current controller and PWM inverter, the output current on ERRF can be controlled as $\mathbf{i}_{\mathbf{dqs}}^{\hat{\mathbf{r}}*}$ regardless of some errors in parameters and estimated angle. And, $\mathbf{i}_{\mathbf{dqs}}^{\mathbf{s}}$ would be regulated as $\mathbf{R}(\hat{\theta}_r)\mathbf{i}_{\mathbf{dqs}}^{\hat{\mathbf{r}}*}$. However, the actual torque of PMSM corresponds to the current on RRF, not ERRF. Therefore, the block diagram from torque reference to output torque can be depicted as Fig. 5.

Fig. 6 illustrates the current vector diagram when an angle error is present. The actual current vector on RRF can be expressed as

$$\mathbf{i}_{\mathbf{dqs}}^{\mathbf{r}} = \mathbf{R}(-\tilde{\theta}_r)\mathbf{i}_{\mathbf{dqs}}^{\hat{\mathbf{r}}} . \tag{15}$$

The PMSM outputs the actual torque corresponding to $\mathbf{i}_{\mathbf{dqs}}^{\mathbf{r}}$, not $\mathbf{i}_{\mathbf{dqs}}^{\hat{\mathbf{r}}}$. Therefore, even if the LUTs for the current reference well-correspond to the torque reference, a torque error can be caused by $\tilde{\theta}_r$ depending on the operating condition.

Fig. 7 (a) and (b) show the torque errors due to angle error in various operating points of an IPMSM and a surface-mounted PMSM (SPMSM), respectively, where the angle errors are assumed as 10° in electrical angle. In Fig. 7 (a), the solid red line represents the desired torque T_e^*, and the magenta dashed line shows the MTPA curve. The dashed arrows are two different current reference vectors, $\mathbf{i}_{\mathbf{dqs,A}}^{\hat{\mathbf{r}}*}$ and $\mathbf{i}_{\mathbf{dqs,B}}^{\hat{\mathbf{r}}*}$, which both can generate T_e^*. $\mathbf{i}_{\mathbf{dqs,A}}^{\hat{\mathbf{r}}*}$ represents the operating point in FW region, while $\mathbf{i}_{\mathbf{dqs,B}}^{\hat{\mathbf{r}}*}$ represents the operating point on the MTPA curve. If there is a positive $\tilde{\theta}_r$, the actual current vectors at RRF would be rotated to $\mathbf{i}_{\mathbf{dqs,A}}^{\mathbf{r}}$ and $\mathbf{i}_{\mathbf{dqs,B}}^{\mathbf{r}}$. Besides, these shifted current vectors cause the torque discrepancy. For example,

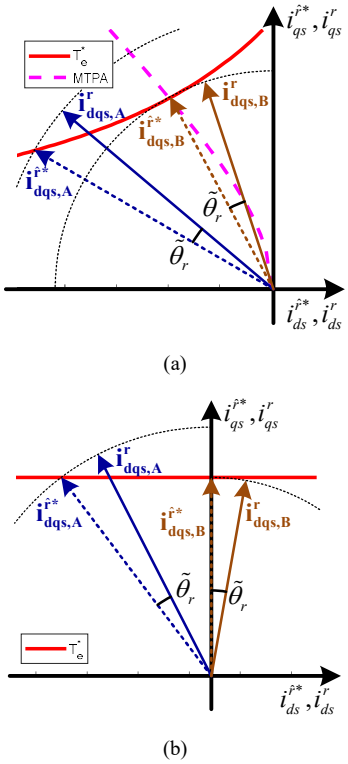

Fig. 7. Torque error due to angle error. (a) IPMSM. (b) SPMSM.

$\mathbf{i}_{\mathbf{dqs,A}}^{\mathbf{r}}$ would produce an excessive torque over T_e^*. On the contrary, T_e would barely differ from T_e^* near MTPA curve, as shown in $\mathbf{i}_{\mathbf{dqs,B}}^{\hat{\mathbf{r}}*}$ and $\mathbf{i}_{\mathbf{dqs,B}}^{\mathbf{r}}$.

Fig. 7 (b) shows the case of SPMSM. As in Fig. 7 (a), $\mathbf{i}_{\mathbf{dqs,A}}^{\hat{\mathbf{r}}*}$ denotes the current reference in the FW region, and $\mathbf{i}_{\mathbf{dqs,B}}^{\hat{\mathbf{r}}*}$ is the reference at the MTPA line which is the q-axis. It can be noted that there is a torque mismatch in the FW region regardless of the saliency of the motor.

The torque discrepancy caused by an angle error which is addressed in Fig. 7 can be quantitatively analyzed through the small-signal modeling. Assuming a small $\tilde{\theta}_r$, the discrepancy between T_e and T_e^* can be deduced as

$$\tilde{T}_e = T_e - T_e^* \approx \frac{dT_e}{d\tilde{\theta}_r}\tilde{\theta}_r \tag{16}$$

In (16), $dT_e / d\tilde{\theta}_r$ can be rewritten in terms of $\mathbf{i}_{\mathbf{dqs}}^{\mathbf{r}}$ as

$$\frac{dT_e}{d\tilde{\theta}_r} = \frac{\partial T_e}{\partial i_{ds}^r}\frac{\partial i_{ds}^r}{\partial \tilde{\theta}_r} + \frac{\partial T_e}{\partial i_{qs}^r}\frac{\partial i_{qs}^r}{\partial \tilde{\theta}_r} . \tag{17}$$

Assuming that the current reference is kept as constant or changes slowly, $\partial i_{ds}^r / \partial \tilde{\theta}_r$ and $\partial i_{qs}^r / \partial \tilde{\theta}_r$ in (17) can be calculated as

$$\frac{\partial i_{ds}^r}{\partial \tilde{\theta}_r} = \frac{\partial}{\partial \tilde{\theta}_r}(i_{ds}^{\hat{r}*}\cos\tilde{\theta}_r + i_{qs}^{\hat{r}*}\sin\tilde{\theta}_r) = i_{qs}^r \tag{18}$$

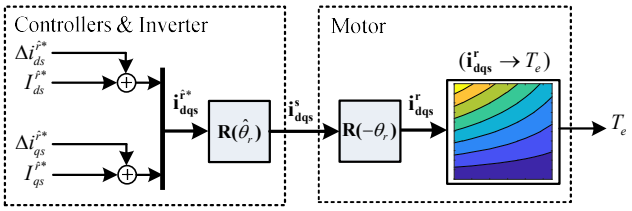

Fig. 8. Modified block diagram of current control and motor considering FW controller's dynamics.

$$\frac{\partial i_{qs}^{r}}{\partial \tilde{\theta}_r} = \frac{\partial}{\partial \tilde{\theta}_r}(-i_{ds}^{\hat{r}*}\sin\tilde{\theta}_r + i_{qs}^{\hat{r}*}\cos\tilde{\theta}_r) = -i_{ds}^{r}. \tag{19}$$

In (18) and (19), it is assumed that the actual current vecter at ERRF tracks well the current reference through the current controller. Applying (18) and (19), (17) can be simplified as

$$\frac{dT_e}{d\tilde{\theta}_r} = \frac{\partial T_e}{\partial i_{ds}^{r}} i_{qs}^{r} - \frac{\partial T_e}{\partial i_{qs}^{r}} i_{ds}^{r}. \tag{20}$$

If the ideal PMSM model is assumed, (20) can be rewritten as

$$\frac{dT_e}{d\tilde{\theta}_r} = 1.5p\left(\Delta L_s\left(i_{qs}^{r\,2} - i_{ds}^{r\,2}\right) - \lambda_f i_{ds}^{r}\right) \tag{21}$$

where $\Delta L_s = L_{ds} - L_{qs}$ and λ_f denotes the flux linkage of the permanent-magnet. L_{ds} and L_{qs} stand for the *d*- and *q*-axis inductances, respectively. Particularly in an ideal SPMSM, $\partial T_e / \partial i_{ds}^{r}$ becomes null due to lack of reluctance torque, and $dT_e / d\tilde{\theta}_r$ can be simplified as

$$\frac{dT_e}{d\tilde{\theta}_r} = -1.5p\lambda_f i_{ds}^{r}. \tag{22}$$

Consequently, in SPMSM, $dT_e / d\tilde{\theta}_r$ is associated with i_{ds}^{r}, not i_{qs}^{r}. In other words, the magnitude of the torque reference does not affect $dT_e / d\tilde{\theta}_r$, and it only depends on how much flux weakening is applied.

C. *Effect of Flux Weakening Controller*

In the previous section, the torque discrepancy due to angle error is analyzed under the assumption of the LUT-based FW control. However, even if the FW control is conducted through a premade LUT, a feedback-type controller, e.g., PI controller, would assist the FW operation to deal with the unknown parameter variation or sensing error [21], [22]. If the PI controller intervenes with the flux weakening, the current reference would be a time varying variable, which might affect the validity of the analysis in (16)-(22). Thus, the current reference variation due to the feedback-type FW controller should be taken into account in analyzing the torque discrepancy.

Regarding the dynamics of a FW controller, the block diagram in Fig. 5 can be modified into Fig. 8. $I_{ds}^{\hat{r}*}$ and $I_{qs}^{\hat{r}*}$ denote the average current references at the certain operating point, and $\Delta i_{ds}^{\hat{r}*}$ and $\Delta i_{qs}^{\hat{r}*}$ represent the small variation of *d*- and *q*-axis current reference due to the dynamics of the FW controller, respectively. Depending on what type of FW controller is adopted, the relation between $\Delta i_{ds}^{\hat{r}*}$ and $\Delta i_{qs}^{\hat{r}*}$ would be determined. The *dq*-axis current reference vector $\mathbf{i}_{\mathbf{dqs}}^{\hat{r}*}$ at ERRF can be represented as follows, considering a small variation of the reference.

$$\mathbf{i}_{\mathbf{dqs}}^{\hat{r}*} = \begin{bmatrix} i_{ds}^{\hat{r}*} \\ i_{qs}^{\hat{r}*} \end{bmatrix} = \begin{bmatrix} I_{ds}^{\hat{r}*} + \Delta i_{ds}^{\hat{r}*} \\ I_{qs}^{\hat{r}*} + \Delta i_{qs}^{\hat{r}*} \end{bmatrix}. \tag{23}$$

Considering a small $\tilde{\theta}_r$, the current vector at RRF can be expressed with the linearized small-signal model as follows.

$$\begin{bmatrix} i_{ds}^{r} \\ i_{qs}^{r} \end{bmatrix} \approx \underbrace{\begin{bmatrix} I_{ds}^{\hat{r}*} \\ I_{qs}^{\hat{r}*} \end{bmatrix}}_{\text{constant values}} + \underbrace{\begin{bmatrix} I_{qs}^{\hat{r}*}\tilde{\theta}_r + \Delta i_{ds}^{\hat{r}*} \\ -I_{ds}^{\hat{r}*}\tilde{\theta}_r + \Delta i_{qs}^{\hat{r}*} \end{bmatrix}}_{\text{small signals}}. \tag{24}$$

From (24), the torque output of a PMSM would be calculated as follows.

$$\begin{aligned} T_e \approx T_e^{*} &+ 1.5p\left(\Delta L_s\left(I_{qs}^{\hat{r}*2} - I_{ds}^{\hat{r}*2}\right) - \lambda_f I_{ds}^{\hat{r}*}\right)\tilde{\theta}_r \\ &+ 1.5p(\lambda_f + \Delta L_s I_{ds}^{\hat{r}*})\Delta i_{qs}^{\hat{r}*} \\ &+ 1.5p\Delta L_s I_{qs}^{\hat{r}*}\Delta i_{ds}^{\hat{r}*}. \end{aligned} \tag{25}$$

Compared to (21), the effects of $\Delta i_{ds}^{\hat{r}*}$ and $\Delta i_{qs}^{\hat{r}*}$ are added in the torque output, and they should be considered in the analysis. However in the SPMSMs, $\Delta i_{qs}^{\hat{r}*}$ can be regarded as null, if a simple FW controller which only changes *d*-axis current reference is applied to the SPMSMs, where the *d*-axis current variation does not affect the torque output. Moreover, since there is no ΔL_s in ideal SPMSMs, the torque output of an ideal SPMSM would be calculated as follows.

$$T_e \approx T_e^{*} - 1.5p\lambda_f I_{ds}^{\hat{r}*}\tilde{\theta}_r. \tag{26}$$

It can be noticed that $\Delta i_{ds}^{\hat{r}*}$ does not appear in (26), and only $I_{ds}^{\hat{r}*}$ is associated with the output torque. It implies that the small variation of $i_{ds}^{\hat{r}*}$ due to the FW controller's dynamics would not affect the torque discrepancy analyzed in Section II. *B*.

D. *Stability Analysis of ESO*

Applying the small-signal modeling of (16), the sensorless torque control loop in Fig. 2 can be transformed into Fig. 9 (a). Focusing on the feedback loop, Fig. 9 (a) can be rearranged into Fig. 9 (b). It can be noticed from Fig. 9 (b) that $dT_e / d\tilde{\theta}_r$ generates the undesired feedback loop (*FB*). By analyzing the loop gain of *FB*, the stability of the sensorless torque control can be evaluated. The loop gain of *FB* can be deduced as

$$T_{FB}(s) = -p\frac{dT_e}{d\tilde{\theta}_r}\frac{1 - H_1(s)}{s\left(J_m s + B_m\right)}. \tag{27}$$

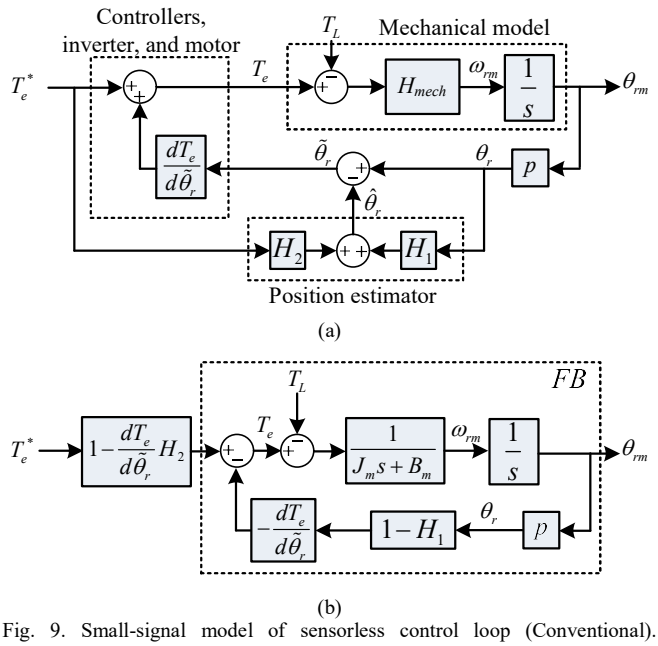

Fig. 9. Small-signal model of sensorless control loop (Conventional). (a) Linearized model. (b) Transformed model with feedback loop, *FB*.

Since T_{FB} contains H_1, the stability of the sensorless torque control would be influenced by the type of position estimator. In the case of ESO, T_{FB} can be deduced as

$$T_{FB,ESO}(s) = -p\frac{dT_e}{d\tilde{\theta}_r}\frac{s\left(\hat{J}_m s+\hat{B}_m\right)}{\left(J_m s+B_m\right)\hat{J}_m H_{ch,ESO}}. \tag{28}$$

It should be noted that the relative degree of $T_{FB,ESO}$ is two. Therefore, for a negative $dT_e/d\tilde{\theta}_r$, the maximum phase delay would not exceed -180°, and the system would always be stable regardless of $dT_e/d\tilde{\theta}_r$. However, when $dT_e/d\tilde{\theta}_r$ is positive, T_{FB} has a negative gain and additional phase delay of -180°, which may cause instability. In (21) and (22), the positive $dT_e/d\tilde{\theta}_r$ region corresponds to the FW region.

The gain margin of $T_{FB,ESO}$ can be evaluated to calculate $dT_e/d\tilde{\theta}_r$ that makes the system unstable. First, the frequency which has -180° of phase delay can be calculated as follows for the system with ESO.

$$\omega_{GM,ESO} = \omega_n\sqrt{\frac{\omega_o}{2\zeta_n\omega_n+\omega_o}}. \tag{29}$$

In (29), $\hat{J}_m$ and $\hat{B}_m$ are assumed to be identical to J_m and B_m, for the sake of simplicity. By applying (29) to (28), the gain margin can be calculated as

$$GM_{ESO} = -20\log\left(\frac{dT_e}{d\tilde{\theta}_r}\frac{p}{J_m\left(2\zeta_n\omega_o\omega_n+\omega_n^2-\omega_{GM,ESO}^2\right)}\right). \tag{30}$$

Therefore, $dT_e/d\tilde{\theta}_r$ to make the system stable can be deduced as

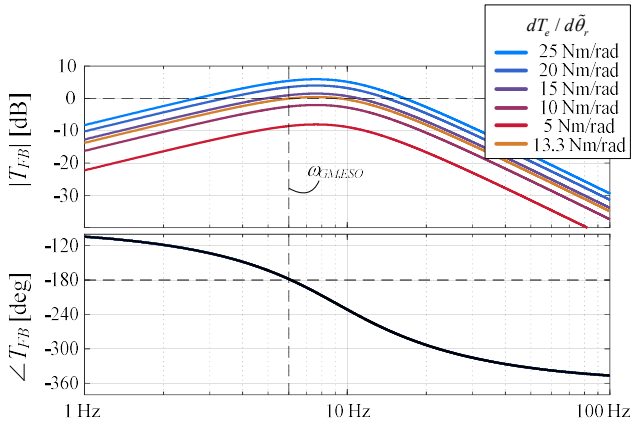

Fig. 10. Bode plot of $T_{FB,ESO}$ for various $dT_e/d\tilde{\theta}_r$ (Conventional).

TABLE I. MOTOR PARAMETERS

Number of pole pair, p	24	
Maximum speed	1500	r/min
Base speed	400	r/min
Rated torque	20	N·m
Rated power	840	W
Rated current	3.2	A_{rms}
Equivalent inertia, J_m	45	g·m^2
Friction constant, B_m	13	mN·m/(rad/s)
Stator inductance, L_s	30	mH
Back-EMF constant, λ_f	0.12	Wb·t

$$\frac{dT_e}{d\tilde{\theta}_r} < \frac{J_m}{p}\left(2\zeta_n\omega_o\omega_n+\omega_n^2-\omega_{GM,ESO}^2\right). \tag{31}$$

In (30) and (31), Since the range of $dT_e/d\tilde{\theta}_r$ is determined by the operating condition, the limit in (31) should be set larger than the expected range of $dT_e/d\tilde{\theta}_r$. When J_m or the gains of ESO are not large enough, the gain margin will decrease, and the system may be unstable. Since J_m and p are the predefined parameters according to the mechanical specification, the only adjustable parameter that can enhance stability is the gains of ESO. However, ω_0, ω_n, and ζ_n are the decisive parameters determining the overall bandwidth of the sensorless control. Larger gains could alleviate the instability theoretically, but they would be limited by the nature of the system, such as noise level or spatial harmonics of the motor under control.

Fig. 10 shows the Bode plots of $T_{FB,ESO}$ for the target SPMSM, of which parameters are in TABLE I. Considering the current limit of the target SPMSM, the maximum limit of $dT_e/d\tilde{\theta}_r$ would be 20 Nm/rad. In Fig. 10, ω_0, ω_n, and ζ_n are set to 72 rad/s, 60 rad/s and 0.7, respectively. As analyzed in (31), increasing $dT_e/d\tilde{\theta}_r$ reduces the gain margin, and the system becomes unstable for $dT_e/d\tilde{\theta}_r$ larger than 13.3 Nm/rad.

III. TORQUE FEEDFORWARD CONSIDERING ANGLE ERROR

A. Stabilization with Modification on Torque Feedforward

For the sensorless control system with ESO, not only H_1 but also H_2 are involved in angle estimation. However, in Fig. 9 (b),

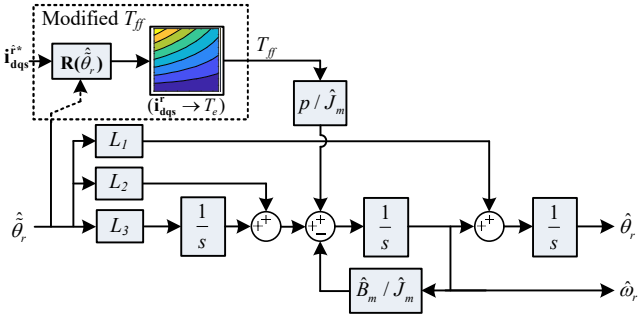

Fig. 11. Position estimator with proposed torque feedforward.

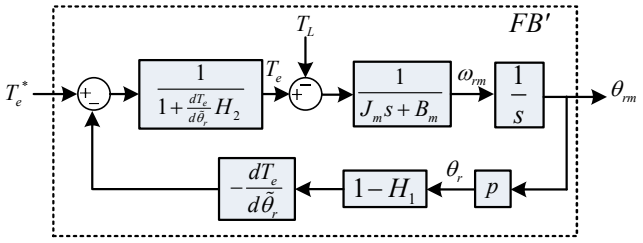

Fig. 12. Sensorless control loop with the proposed torque feedforward.

H_2 is located outside of the feedback loop, and it does not contribute to enhancing stability. It is because T_{ff} is set to T_e^*, and does not reflect the torque discrepancy due to $\tilde{\theta}_r$. If T_{ff} is modified considering $\tilde{\theta}_r$, the stability of the sensorless torque control could be improved.

Conventionally, the torque feedforward is the same as torque reference. If the current reference generator is based on the accurate motor parameters and the current reference is well-regulated, the conventional torque feedforward $T_{ff,\text{conv}}$ can be rewritten with the current reference at ERRF as

$$T_{ff,\text{conv}} = T_e^* = \tau(i_{ds}^{r*}, i_{qs}^{r*}) \tag{32}$$

where $\tau(i_{ds}^r, i_{qs}^r)$ denotes the output torque corresponding to $\mathbf{i}^{\mathbf{r}}_{\mathbf{dqs}}$. The actual torque can be calculated with dq-axes currents at RRF as follows.

$$T_e = \tau(i_{ds}^r, i_{qs}^r). \tag{33}$$

Unfortunately, it is not easy to apply $\tau(i_{ds}^r, i_{qs}^r)$ to T_{ff} directly, because $\mathbf{i}^{\mathbf{r}}_{\mathbf{dqs}}$ is unknown in sensorless control. Instead, the estimated current at RRF $\hat{\mathbf{i}}^{\mathbf{r}}_{\mathbf{dqs}}$ can be calculated from $\mathbf{i}^{\mathbf{r}}_{\mathbf{dqs}}$ and $\hat{\tilde{\theta}}_r$ as follows.

$$\hat{\mathbf{i}}^{\mathbf{r}}_{\mathbf{dqs}} = \mathbf{R}(\hat{\tilde{\theta}}_r) \cdot \mathbf{i}^{\hat{\mathbf{r}}}_{\mathbf{dqs}}. \tag{34}$$

$\hat{\tilde{\theta}}_r$ is the estimated angle error which is obtained from the sensorless observer. The block diagram of the proposed estimator is illustrated in Fig. 11. The proposed torque feedforward $T_{ff,\text{prop}}$ can be obtained from the torque equation as follows.

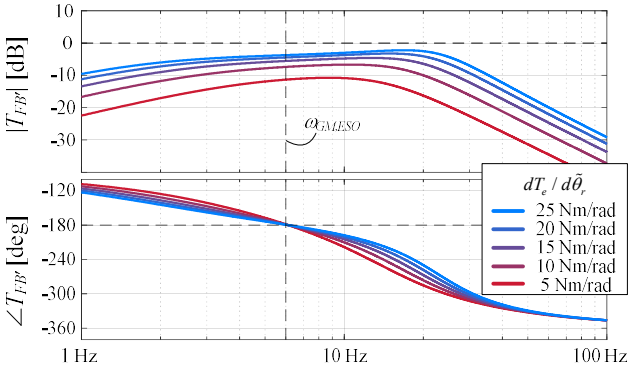

Fig. 13. Bode plot of $T_{FB'}$ for various $dT_e / d\tilde{\theta}_r$ (Proposed).

$$T_{ff,\text{prop}} = \tau(\hat{i}_{ds}^r, \hat{i}_{qs}^r) = 1.5p\left(\hat{\lambda}_f + \Delta\hat{L}_s \hat{i}_{ds}^r\right)\hat{i}_{qs}^r. \tag{35}$$

In the case of a magnetically saturated PMSM, the torque equation using constant motor parameters in (35) might not reflect the actual torque precisely. To avoid the torque mismatch due to magnetic saturation, $T_{ff,\text{prop}}$ can be calculated from $\hat{\mathbf{i}}^{\mathbf{r}}_{\mathbf{dqs}}$ using the LUT, which would be the table used in the control loop in Fig. 5.

Fig. 12 depicts the modified control loop with the proposed torque feedforward. The difference from the conventional control loop in Fig. 9 (b) is the location of H_2. Unlike Fig. 9 (b), an additional transfer function $1/(1+\frac{dT_e}{d\tilde{\theta}_r}H_2)$ is inside the new feedback loop FB', and the loop gain can be reformed as

$$T_{FB',ESO}(s) = -p\frac{dT_e}{d\tilde{\theta}_r}\frac{s\left(\hat{J}_m s + \hat{B}_m\right)}{\left(1+\frac{dT_e}{d\tilde{\theta}_r}H_2\right)\left(J_m s + B_m\right)\hat{J}_m H_{ch,ESO}}. \tag{36}$$

The Bode plot of (36) is shown in Fig. 13. When $dT_e / d\tilde{\theta}_r$ is 5 Nm/rad, the shape of the FB' is quite similar to that in Fig. 10. However, unlike the conventional torque feedforward, the gain margin is secured even when $dT_e / d\tilde{\theta}_r$ increases. In (36), $\omega_{GM,ESO}$ is identical to (29), and the gain margin is reformed as

$$GM_{ESO} = -20\log\left(\frac{\frac{dT_e}{d\tilde{\theta}_r}}{\frac{J_m}{p}\left(2\zeta_n\omega_o\omega_n + \omega_n^2 - \omega_{GM,ESO}^2\right) + \frac{dT_e}{d\tilde{\theta}_r}\omega_{GM,ESO}}\right). \tag{37}$$

In (37), no matter how large $dT_e / d\tilde{\theta}_r$ is, the gain margin has the lower bound of 20 $\log(\omega_{GM,ESO})$. Since $\omega_{GM,ESO}$ in (29) would be larger than 1 rad/s, the modified torque feedforward secures the stability of the system regardless of the magnitude of $dT_e / d\tilde{\theta}_r$.

B. Effect of Noise in Sensorless Observer

$\hat{\tilde{\theta}}_r$ is the signal obtained from the voltage and current information, and it is usually a raw signal with a lot of noise. The position estimator tracks the rotor position rejecting high

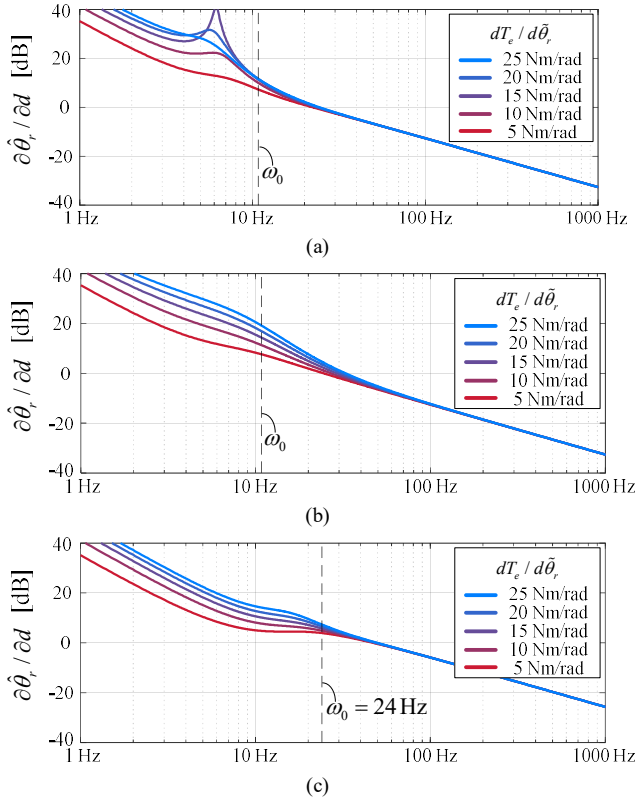

Fig. 14. Noise susceptibility in $\hat{\theta}_r$.
(a) Conventional control loop. (b) Proposed control loop. (c) Conventional control loop with increased bandwidth.

frequency noise in $\hat{\tilde{\theta}}_r$. Observing Fig. 11, the proposed method exploits $\hat{\tilde{\theta}}_r$ as a feedforwarding value without filtering, and there may be concerns that the proposed method would be vulnerable to the noise of the system, such as current sensing noise.

In order to analyze the effect of noise in the angle estimation, the noise susceptibility in $\hat{\theta}_r$ is calculated for both systems. Considering a noise d in the sensorless observer, $\hat{\tilde{\theta}}_r$ can be replaced as

$$\hat{\tilde{\theta}}_r = \tilde{\theta}_r + d \,. \tag{38}$$

For the conventional control loop in Fig. 9, the small-signal gain from d to $\hat{\theta}_r$ is illustrated in Fig. 14 (a). It has a resonance around 6 Hz for the high $dT_e / d\tilde{\theta}_r$, and it decreases with the slope of -20 dB/dec. Meanwhile, Fig. 14 (b) shows the noise susceptibility of the proposed system. With the proposed torque feedforward, the resonance has been resolved while keeping the noise susceptibility in high frequency region at the same level. It should be noted that the effect of d also decreases with -20 dB/dec above ω_0. Therefore, the proposed system has reasonably strong immunity for the high-frequency noise, similar to the conventional method.

As analyzed in Section II. *C*, without applying the proposed method, the stability can be enhanced by simply increasing the

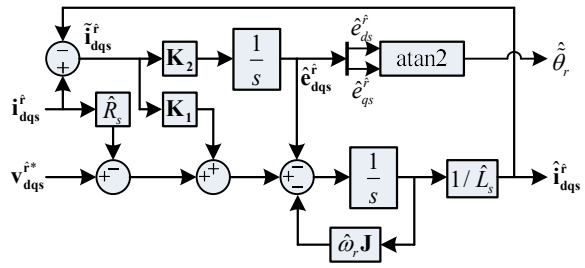

Fig. 15. Block diagram of sensorless observer in [12].

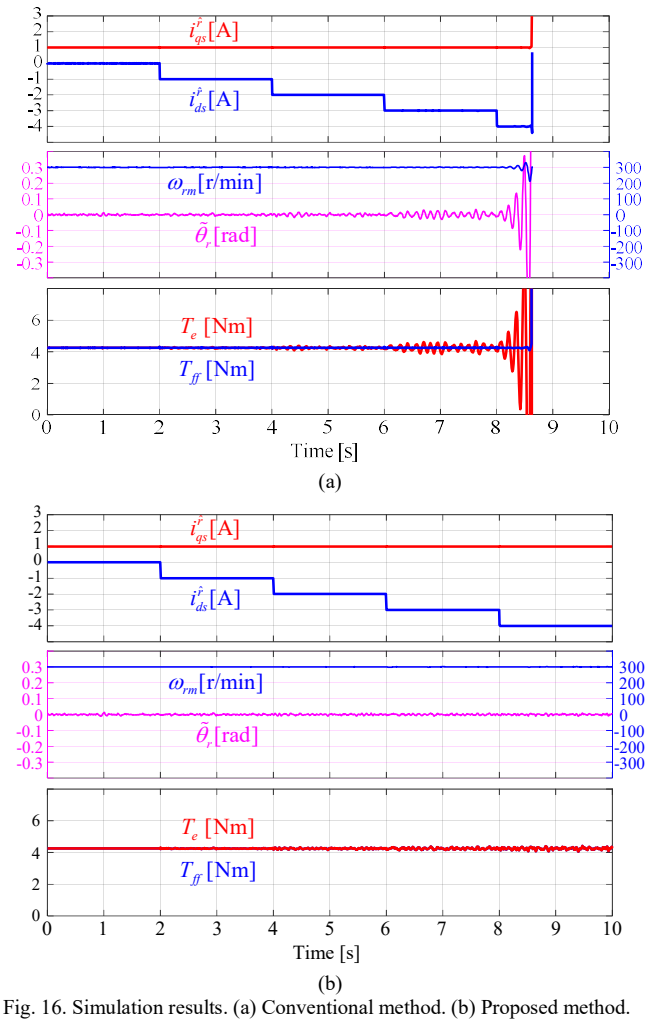

Fig. 16. Simulation results. (a) Conventional method. (b) Proposed method.

gains of position estimator. Fig. 14 (c) depicts the noise susceptibility of the conventional control loop with increased gain, which is set to ω_0 =150 rad/s and ω_n =125 rad/s. Similar to the proposed method, the increased gain reduces the resonance and the instability has been resolved. However, unlike the proposed method, the noise susceptibility is worsened in overall frequencies, including the high-frequency region.

IV. Simulation and Experimental Results

To verify the analysis and the effectiveness of the proposed method, the simulation and experiments have been conducted.

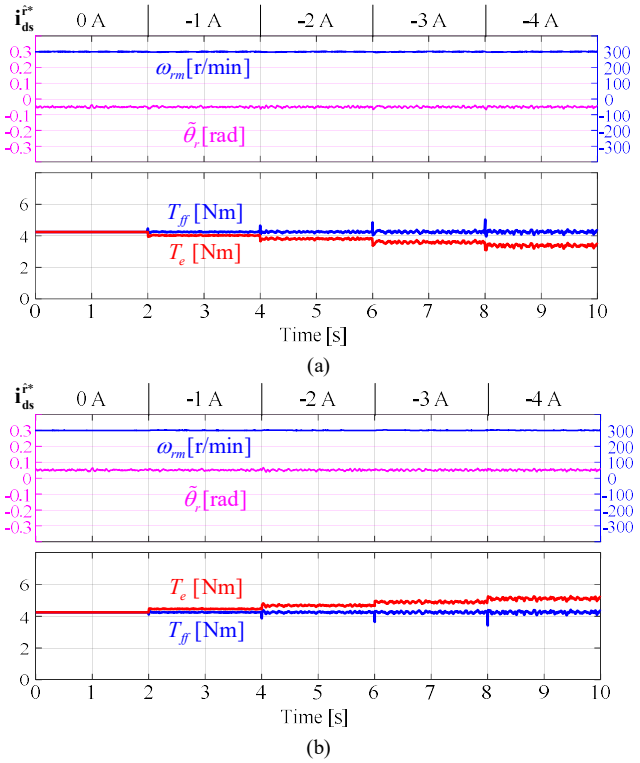

Fig. 17. Proposed method under L_s error (Simulation).
(a) Underestimated case (0.8 L_s). (b) Overestimated case (1.2 L_s).

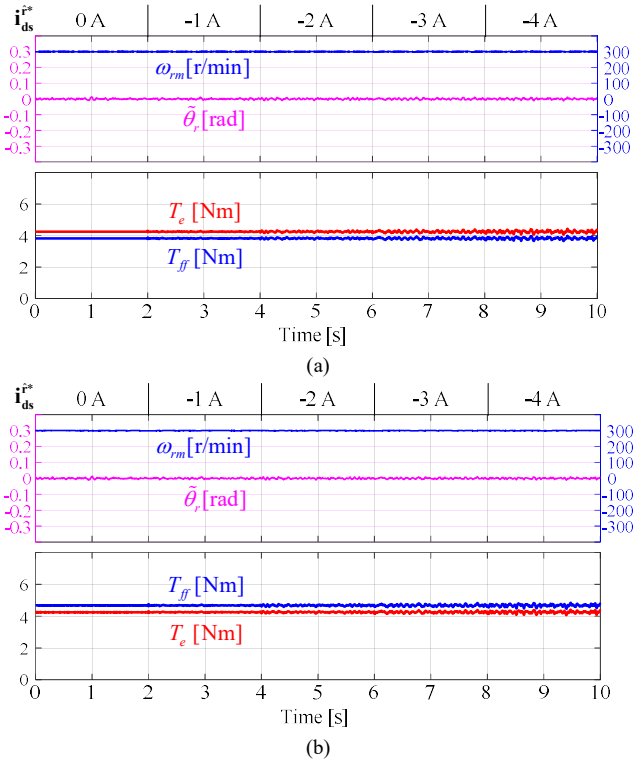

Fig. 18. Proposed method under λ_f error (Simulation).
(a) Underestimated case (0.9 λ_f). (b) Overestimated case (1.1 λ_f).

The SPMSM in TABLE I is selected as the target motor, and the observer gains are also set as listed in Section II. *C*. The state feedback type current controller has been adopted, and its bandwidth is set to 200 Hz for both simulation and experimental setup. The switching frequency of the voltage source inverter (VSI) is set to 10 kHz, and the current sensing and PWM update are conducted twice per every switching period.

For the sensorless observer, the full-order observer in [11] and [12] has been implemented. The block diagram of the sensorless observer in [12] is depicted in Fig. 15. It is constructed on ERRF, and it estimates the back-EMF vector $\hat{\mathbf{e}}^{\hat{\mathbf{r}}}_{\mathbf{dqs}}$. $\hat{\tilde{\theta}}_r$ is obtained by applying arctangent operation to $\hat{\mathbf{e}}^{\hat{\mathbf{r}}}_{\mathbf{dqs}}$.

$\mathbf{K_1}$ and $\mathbf{K_2}$ are the two by two gain matrices determining the bandwidth of the sensorless observer, which is set to 800 Hz in this paper. Since the bandwidth of the sensorless observer is much higher than that of the position estimator, it can be assumed that the estimated angle error has no delay in terms of the position estimator. Therefore, H_{SL} can be treated as unity, where there is no parameter error.

A. Simulation Results

Fig. 16 depicts the simulation results for the target motor. The motor operates with constant $i^{\hat{r}*}_{qs}$ with 1 A, varying $i^{\hat{r}*}_{ds}$ from 0 A to -4 A. And the load machine regulates the speed at 300 r/min with low control bandwidth, which is 1 Hz. The mechanical system with low bandwidth of speed control can be modeled as free inertia with friction in the small-signal model while keeping the average speed. For the proposed torque feedforward, the torque equation in (35) has been adopted for the sake of simplicity.

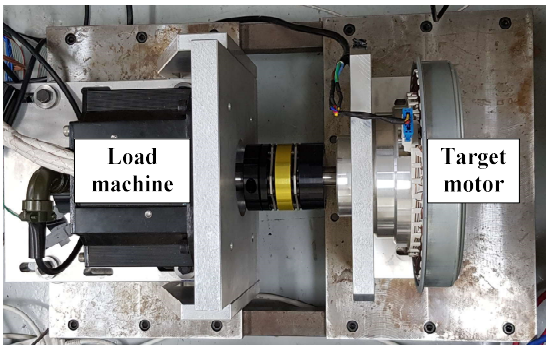

Fig. 19. Experimental setup.

As analyzed in Section II. *C*, in Fig. 16 (a), the angle estimation fails, and the instability is caused in the deep FW region. When $i^{\hat{r}*}_{ds}$ is -4 A, $dT_e / d\tilde{\theta}_r$ is expected to be 17.25 Nm/rad, which exceeds the limit of the stability condition in Fig. 10. Because of the severe angle estimation error, the output torque also loses its control and the mechanical speed oscillates. On the other hand, in Fig. 16 (b), the proposed system keeps stable even in the deep FW region. In addition, even when $i^{\hat{r}*}_{ds}$ is larger than -4 A, the ripple in the angle estimation error is reduced compared to the conventional method.

To see the effects of parameter errors on the proposed method, 20 % of L_s error and 10 % of λ_f error have been applied in Fig. 17 and Fig. 18. The current references are set equal to those in Fig. 16. In Fig. 17 (a) and (b), despite the inductance error and the resulting angle error, the proposed torque feedforward helps the system keep stable. Fig. 18 (a) and (b) show the simulation results under the error in λ_f. Since the sensorless observer in [12] does not use λ_f information, the λ_f

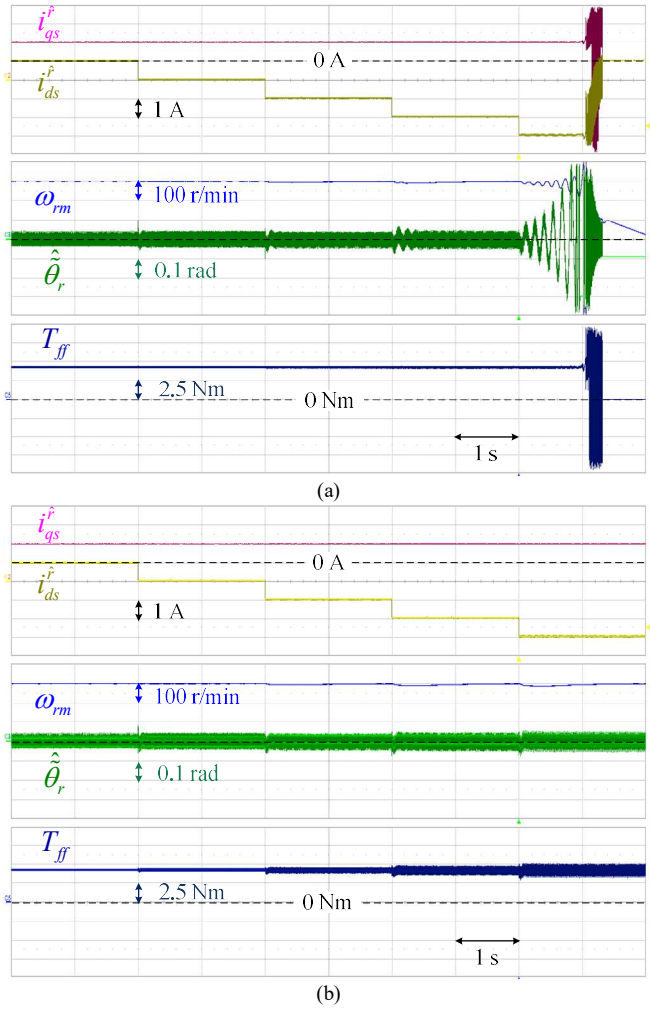

Fig. 20. Experimental results. (a) Conventional method. (b) Proposed method.

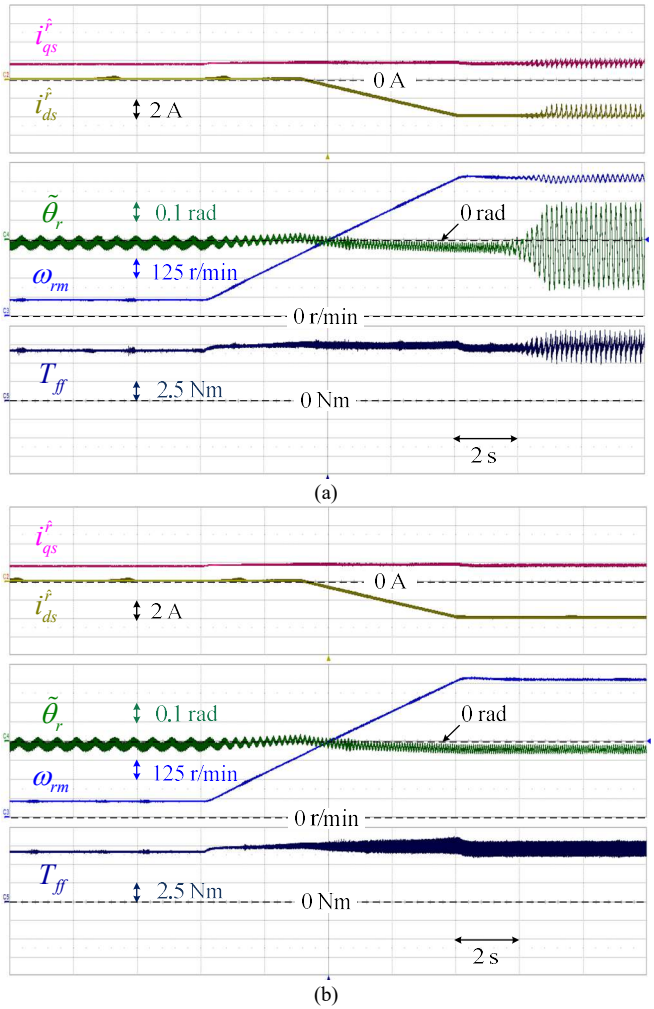

Fig. 21. Experimental results of speed control with LUT-based FW control. (a) Conventional method. (b) Proposed method.

error only induces the error in the scale of T_{ff}. Although the λ_f error causes the dc error in torque feedforward, the system still keeps the stability regardless of the direction of λ_f error.

B. Experimental Results

The motor-generator set used in the experiments is shown in Fig. 19. The specification of the target motor is the same as the simulation, and 3.9 kW SPMSM is selected for the load machine. The proposed control algorithms are implemented on TMS320F28377 DSP board, and the phase current and dc-link voltage are measured through 16 bit A/D converter.

The experimental results corresponding to the simulation are depicted in Fig. 20. The shaft speed is regulated at 300 r/min by the load machine, and the *q*-axis current reference is set to 1 A. As in the simulation, the conventional system loses control at $i^{\hat{r}*}_{ds}$ = -4 A in Fig. 20 (a). Besides, when $i^{\hat{r}*}_{ds}$ = -3 A, it is not unstable but $\hat{\tilde{\theta}}_r$ is oscillatory in transient. It can be noticed that $\hat{\tilde{\theta}}_r$ in experimental results is much noisier than that in the simulation. It would be the noise *d* of the sensorless observer in Fig. 2, which might be from the current sensing noise or the spatial harmonics of the motor.

On the other hand, Fig. 20 (b) shows the experimental results of the proposed method. Unlike the conventional torque feedforward, T_{ff} in Fig. 20 (b) has a ripple in FW region to compensate the torque error due to $\tilde{\theta}_r$. This ripple not only stabilizes the system when $i^{\hat{r}*}_{ds}$ = -4 A, but also reduces the oscillation when $i^{\hat{r}*}_{ds}$ = -3 A.

Since the speed control is the outer loop, in which the torque control is inside, the instability of torque control loop also adversely affects the speed control, as shown in Fig. 21. The load torque of 7 Nm is applied by the load machine, and the target motor accelerates from 100 r/min to 900 r/min. In Fig. 21, the LUT-based FW control has been conducted. In FW region, the *d*-axis current increases in negative direction. In Fig. 21 (a), the system has the resonance, and it loses control at 900 r/min, while the proposed torque feedforward stabilizes the system as depicted in Fig. 21 (b).

As analyzed in Section II. *C*, even if the feedback-type FW controller is applied, the instability phenomenon would still remain. Fig. 22 shows the experimental results with the feedback-type FW control. The operating conditions are the same as those in Fig. 21 except the FW controller. A simple PI-controller in Fig. 23 is used for FW operation. V_{lim} denotes the limit of the output voltage, and I_{max} denotes the magnitude of the maximum output current. Similar to LUT-based FW control,

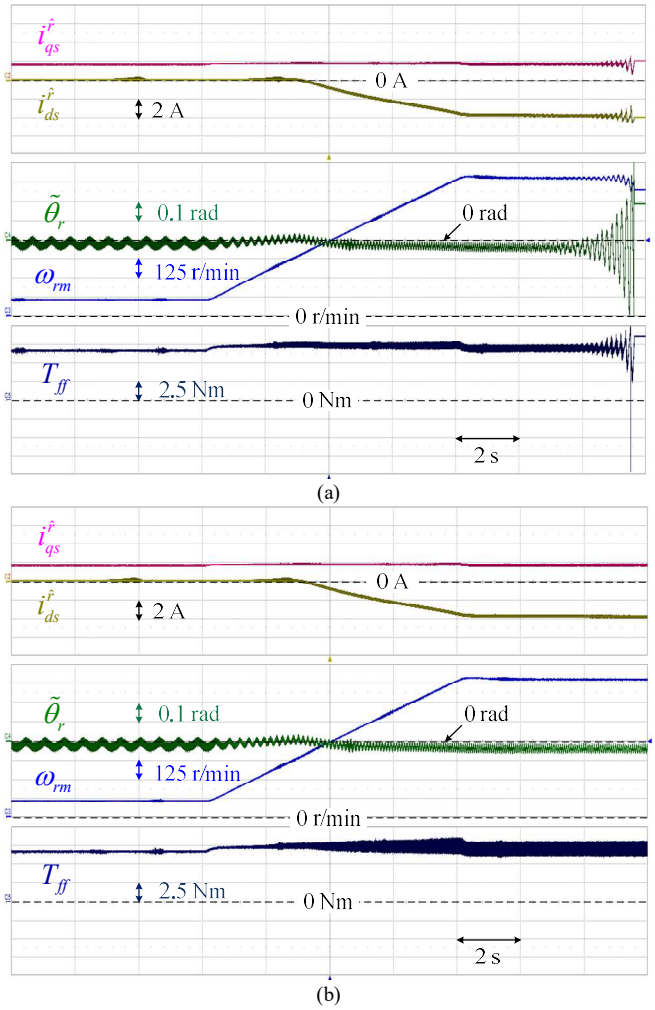

Fig. 22. Experimental results of speed control with feedback-type FW control. (a) Conventional method. (b) Proposed method.

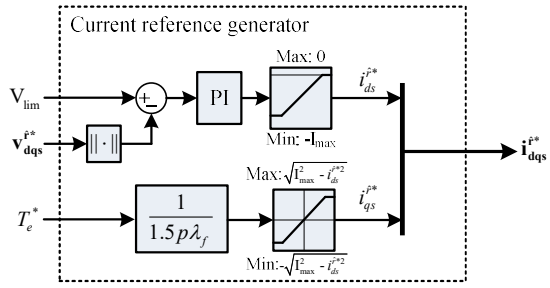

Fig. 23. Feedback-type FW controller used in experiments.

the conventional control algorithm loses its stability in the deep flux weakening region. And, it can be noted that the proposed method is still effective in stabilizing the control system in the flux weakening region regardless of the method of the FW control.

V. Conclusion

This paper analyzes the torque control stability in sensorless PMSM drives. Due to inevitable angle estimation error in sensorless control, there is a difference between the actual torque and the reference. This torque error deteriorates the stability of the torque control loop in the flux-weakening region. This phenomenon can be more severe in low-inertia applications. To migrate this instability, it is proposed to modify the torque feedforward term considering angle estimation error. The proposed compensation ensures the stability of the system without increasing the gains of the observer, which helps to keep the same noise immunity in the high-frequency region as the conventional system. The simulation and experimental results verify the feasibility of the proposed method.

Acknoledgement

This work was supported in part by Seoul National University Electric Power Research Institue, in part by the Hyundai Motor Chung Mong-Koo Foundation, and in part by Brain Korea 21 Plus Project in 2020, granted financial resource from the Ministry of Trade, Industry, and Energy, Republic of Korea.

References

[1] P. Vadstrup and R. D. Lorenz, "Robust estimator design for signal injection-based IPM synchronous machine drives," *Conference Record of the 2004 IEEE Industry Applications Conference, 2004. 39th IAS Annual Meeting.*, Seattle, WA, USA, 2004, pp. 957-963 vol.2, doi: 10.1109/IAS.2004.1348529.

[2] Y. Yoon, S. Sul, S. Morimoto and K. Ide, "High-Bandwidth Sensorless Algorithm for AC Machines Based on Square-Wave-Type Voltage Injection," in *IEEE Transactions on Industry Applications*, vol. 47, no. 3, pp. 1361-1370, May-June 2011, doi: 10.1109/TIA.2011.2126552.

[3] Q. Tang, A. Shen, X. Luo and J. Xu, "PMSM Sensorless Control by Injecting HF Pulsating Carrier Signal Into ABC Frame," in *IEEE Transactions on Power Electronics*, vol. 32, no. 5, pp. 3767-3776, May 2017, doi: 10.1109/TPEL.2016.2583787.

[4] Y. Kwon, J. Lee and S. Sul, "Extending Operational Limit of IPMSM in Signal-Injection Sensorless Control by Manipulation of Convergence Point," in *IEEE Transactions on Industry Applications*, vol. 55, no. 2, pp. 1574-1586, March-April 2019, doi: 10.1109/TIA.2018.2882483.

[5] J. M. Liu and Z. Q. Zhu, "Novel Sensorless Control Strategy With Injection of High-Frequency Pulsating Carrier Signal Into Stationary Reference Frame," in *IEEE Transactions on Industry Applications*, vol. 50, no. 4, pp. 2574-2583, July-Aug. 2014, doi: 10.1109/TIA.2013.2293000.

[6] J. Lee, Y. Kwon and S. Sul, "Analysis of Position Control Stability Affected by Non-ideal Characteristics of IPMSM in Signal-Injection Sensorless Control," *2019 IEEE Energy Conversion Congress and Exposition (ECCE)*, Baltimore, MD, USA, 2019, pp. 785-791, doi: 10.1109/ECCE.2019.8912799.

[7] G. Zhang, G. Wang, B. Yuan, R. Liu and D. Xu, "Active Disturbance Rejection Control Strategy for Signal Injection-Based Sensorless IPMSM Drives," in *IEEE Transportation Electrification*, vol. 4, no. 1, pp. 330-339, March 2018, doi: 10.1109/TTE.2017.2765206.

[8] A. Yousefi-Talouki, P. Pescetto and G. Pellegrino, "Sensorless Direct Flux Vector Control of Synchronous Reluctance Motors Including Standstill, MTPA, and Flux Weakening," in *IEEE Transactions on Industry Applications*, vol. 53, no. 4, pp. 3598-3608, July-Aug. 2017, doi: 10.1109/TIA.2017.2679689.

[9] S. Morimoto, K. Kawamoto, M. Sanada and Y. Takeda, "Sensorless control strategy for salient-pole PMSM based on extended EMF in rotating reference frame," in *IEEE Transactions on Industry Applications*, vol. 38, no. 4, pp. 1054-1061, July-Aug. 2002, doi: 10.1109/TIA.2002.800777.

[10] N. Matsui, "Sensorless PM brushless DC motor drives," in *IEEE Transactions on Industrial Electronics*, vol. 43, no. 2, pp. 300-308, April 1996, doi: 10.1109/41.491354.

[11] J. Yoo, Y. Lee and S. Sul, "Back-EMF Based Sensorless Control of IPMSM with Enhanced Torque Accuracy Against Parameter Variation," *2018 IEEE Energy Conversion Congress and Exposition (ECCE)*, Portland, OR, 2018, pp. 3463-3469, doi: 10.1109/ECCE.2018.8557803.

[12] Yo-Chan Son, Bon-Ho Bae and Seung-Ki Sul, "Sensorless operation of permanent magnet motor using direct voltage sensing circuit," *Conference Record of the 2002 IEEE Industry Applications Conference. 37th IAS Annual Meeting (Cat. No.02CH37344)*, Pittsburgh, PA, USA, 2002, pp. 1674-1678 vol.3, doi: 10.1109/IAS.2002.1043759.

[13] Y. Lee, Y. Kwon and S. Sul, "Comparison of rotor position estimation performance in fundamental-model-based sensorless control of PMSM," *2015 IEEE Energy Conversion Congress and Exposition (ECCE)*, Montreal, QC, 2015, pp. 5624-5633, doi: 10.1109/ECCE.2015.7310451.

[14] Z. Xu, T. Zhang, Y. Bao, H. Zhang and C. Gerada, "A Nonlinear Extended State Observer for Rotor Position and Speed Estimation for Sensorless IPMSM Drives," in *IEEE Transactions on Power Electronics*, vol. 35, no. 1, pp. 733-743, Jan. 2020, doi: 10.1109/TPEL.2019.2914119.

[15] Y. Lee and S. Sul, "Model-Based Sensorless Control of an IPMSM With Enhanced Robustness Against Load Disturbances Based on Position and Speed Estimator Using a Speed Error," in *IEEE Transactions on Industry Applications*, vol. 54, no. 2, pp. 1448-1459, March-April 2018, doi: 10.1109/TIA.2017.2777390.

[16] R. D. Lorenz and K. W. Van Patten, "High-resolution velocity estimation for all-digital, AC servo drives," in *IEEE Transactions on Industry Applications*, vol. 27, no. 4, pp. 701-705, July-Aug. 1991, doi: 10.1109/28.85485.

[17] Hyunbae Kim, M. C. Harke and R. D. Lorenz, "Sensorless control of interior permanent-magnet machine drives with zero-phase lag position estimation," in *IEEE Transactions on Industry Applications*, vol. 39, no. 6, pp. 1726-1733, Nov.-Dec. 2003, doi: 10.1109/TIA.2003.818966.

[18] S. Bolognani, S. Calligaro and R. Petrella, "Design Issues and Estimation Errors Analysis of Back-EMF-Based Position and Speed Observer for SPM Synchronous Motors," in *IEEE Journal of Emerging and Selected Topics in Power Electronics*, vol. 2, no. 2, pp. 159-170, June 2014, doi: 10.1109/JESTPE.2013.2296974.

[19] J. Yoo and S. Sul, "Analysis of Torque Control Stability of PMSM Sensorless Drives in Flux Weakening Region," presented in *2020 IEEE International Power Electronics and Motion Control Conference (IPEMC 2020-ECCE Asia)*, Nanjing, China, Nov. 29-Dec. 2, 2020.

[20] M. Tursini, E. Chiricozzi and R. Petrella, "Feedforward Flux-Weakening Control of Surface-Mounted Permanent-Magnet Synchronous Motors Accounting for Resistive Voltage Drop," in *IEEE Transactions on Industrial Electronics*, vol. 57, no. 1, pp. 440-448, Jan. 2010, doi: 10.1109/TIE.2009.2034281.

[21] B. Bae, N. Patel, S. Schulz and S. Sul, "New field weakening technique for high saliency interior permanent magnet motor," *38th IAS Annual Meeting on Conference Record of the Industry Applications Conference*, 2003., Salt Lake City, UT, USA, 2003, pp. 898-905 vol.2, doi: 10.1109/IAS.2003.1257641.

[22] N. Bedetti, S. Calligaro and R. Petrella, "Analytical Design and Autotuning of Adaptive Flux-Weakening Voltage Regulation Loop in IPMSM Drives With Accurate Torque Regulation," in *IEEE Transactions on Industry Applications*, vol. 56, no. 1, pp. 301-313, Jan.-Feb. 2020, doi: 10.1109/TIA.2019.2942807.

Jiwon Yoo (S'17) was born in Seoul, South Korea in 1990. He received the B.S. degree in electrical engineering from Seoul National University, Seoul, South Korea in 2017, where he is currently pursuing the Ph.D. degree in electrical engineering. From 2014 to 2017, He was a Research Engineer with Seoho Electric Company, Anyang, South Korea. His current research interests include power electronics, control of electric machines, power semiconductors, and sensorless drives.

He was the recipient of the Best Paper Award First Prize at 2019 International Conference on Power Electronics (ICPE-Busan/ECCE-Asia) and the Best Paper Award at 2020 International Power Electronics and Motion Control Conference (IPEMC-Nanjing/ECCE-Asia).

Joohyun Lee (S'16) was born in Anyang, Korea in 1992. She received the B.S. degree in electrical engineering from Seoul National University, Seoul, South Korea in 2015, where she is currently pursuing the Ph.D. degree in electrical engineering. Her current research interests include power electronics, control of electric machines and converters, electric/hybrid vehicles, and sensorless drive.

She was the recipient of the Best Paper Award First Prize at 2019 International Conference on Power Electronics (ICPE-Busan/ECCE-Asia).

Seung-Ki Sul (S'78–M'87–SM'98–F'00) received the B.S., M.S., and Ph.D. degrees in electrical engineering from Seoul National University, Seoul, South Korea, in 1980, 1983, and 1986, respectively.

From 1986 to 1988, he was an Associate Researcher with the Department of Electrical and Computer Engineering, University of Wisconsin, Madison, WI, USA. From 1988 to 1990, he was a Principal Research Engineer with LG Industrial Systems Company, South Korea. Since 1991, he has been a member of faculty with the School of the Electrical and Computer Engineering, Seoul National University, where he is currently a Professor. He has authored or coauthored more than 150 IEEE journal papers and a total of more than 340 international conference papers in the area of power electronics. His current research interests include position sensorless control of electrical machines, electric/hybrid vehicles and ship drives, and power-converter circuits based on SiC MOSFET.

Dr. Sul was the Program Chair of IEEE Power Electronics Specialists Conference in 2006 and the General Chair of IEEE International Conference on Power Electronics and ECCE-Asia in 2011. From 2011 to 2014, he was the Editor-in Chief for the Journal of Power Electronics, which is an SCIE-registered journal, published by the Korean Institute of Power Electronics (KIPE), Seoul, South Korea. For year 2015, he was the President of KIPE. He was the recipient of the 2015 IEEE Transaction 1st and 2nd Paper Awards on Industrial Application, simultaneously. He was also the recipient of the 2016 Outstanding Achievement Award of the IEEE Industrial Application Society. He was also selected as the recipient of the 2017 Newell award sponsored by IEEE Power Electronics Society.